Additive Manufacturing of Steels

Contents

Introduction

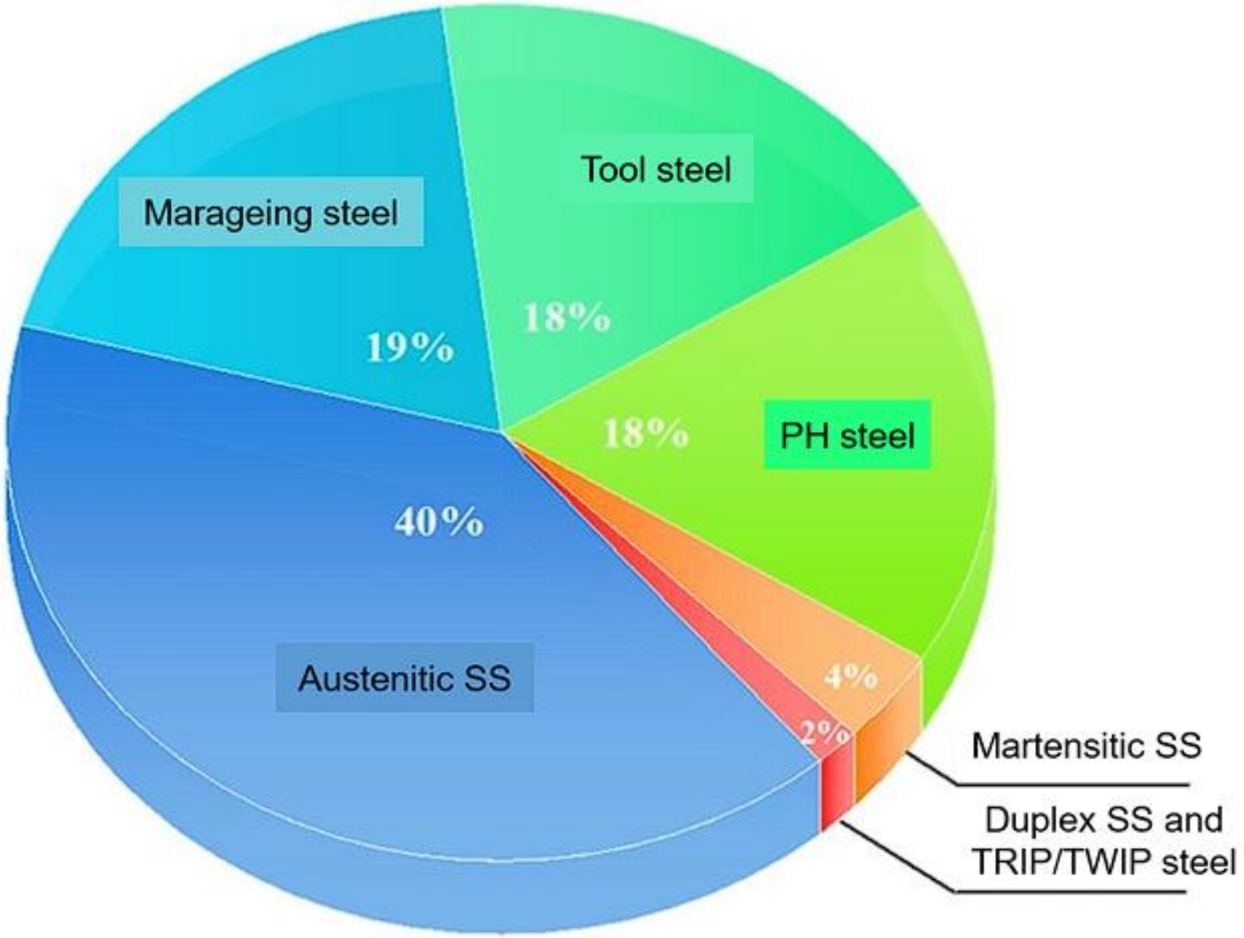

Figure 1.1: Percentage of research work on AM of various steel categories. Adopted from [4].

Introduction

Table 1.1: The nominal composition of the most commonly AMed steels. All compositions are in weight percent, and the Fe content is balanced.

Alloy	Category	C	Cr	Ni	Mo	Mn	Si	Other
316L	Austenitic SS	<0.03	16-18	10-14	2-2.5	<2	<0.75	-
304L	Austenitic SS	<0.03	17.5-19.5	8-10.5	-	<2	<1	-
18Ni-300	Marageing steel	<0.03	<0.5	17-19	4.5-5.2	<0.1	<0.1	0.6-0.8 Ti, 0.05-0.15 Al, 8.5-9.5 Co
17-4	PH steel	<0.07	15-17	3-5	-	1	1	3-5 Cu
15-5	PH steel	<0.07	14-15.5	3.5-5.5	-	<1	<1	2.5-4.5 Cu, 0.15-0.45 Nb
H13	Tool steel	0.32-0.45	4.75-5.5	-	1.1-1.75	0.2-0.6	0.8-1.2	0.8-1.2 V
SAF2205	Duplex SS	<0.03	25	7	4	<1.2	<0.8	

Austenitic stainless steels

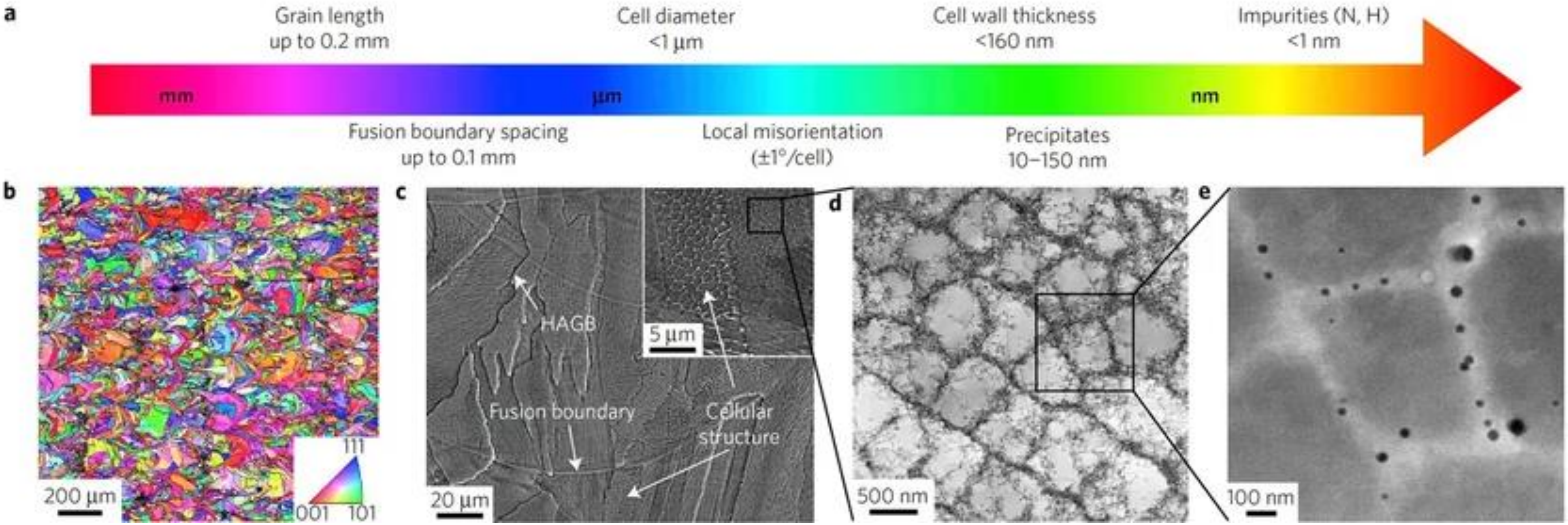

Fig. Microstructure of LPBFed 316L steel at various length scales: (a) various length scales of the observed microstructural features, (b) grain orientations are depicted using EBSD inverse pole figure mapping, (c) SEM image of a cross section demonstrating HAGB, fusion boundaries (delineating melt pools), and a cellular solidification structure (d) bright field TEM image of the cellular structure revealing dislocation networks at cell boundaries, and (e) scanning TEM (STEM) image of the solidification cells with high-angle annular dark-field (HAADF) oxide particles

Source: Wang et al. 2018 [https://doi.org/10.1038/nmat5021]

Austenitic stainless steels

Fig. (a) STEM/EDS elemental maps of cellular structure, (b) EDS line analysis along the white dashed line, (c) CALPHAD simulation of changes in Cr distribution through a cell wall as a function of annealing temperature for a 1 hour holding time. The fitted experimental data shown in b is the starting profile of the as-built material (red curve), and (d) Calculated differences in Cr and Mo content between cell walls and cell interiors as a function of annealing temperature for various holding times. The star symbols indicate the simulated temperatures

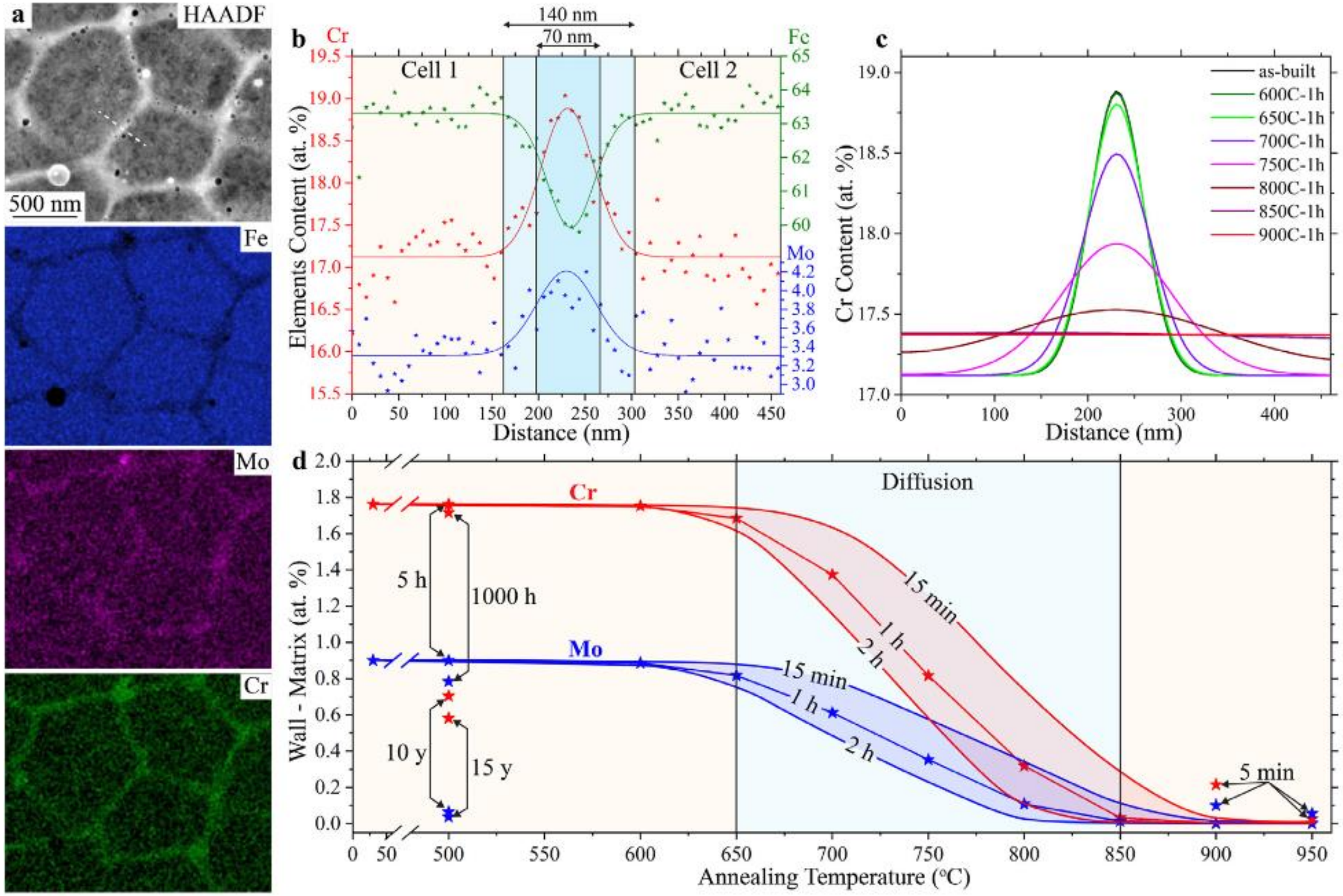

Source: Voisin et al 2021 [https://doi.org/10.1016/j.actamat.2020.11.018]

Austenitic stainless steels

Fig. (a), (b) Bright field TEM micrographs of as built LPBFed 316L SS processed with various processing parameters, and (c), (d) Selected area diffraction pattern (SADP) corresponding to (a) and (b) TEM micrographs, respectively

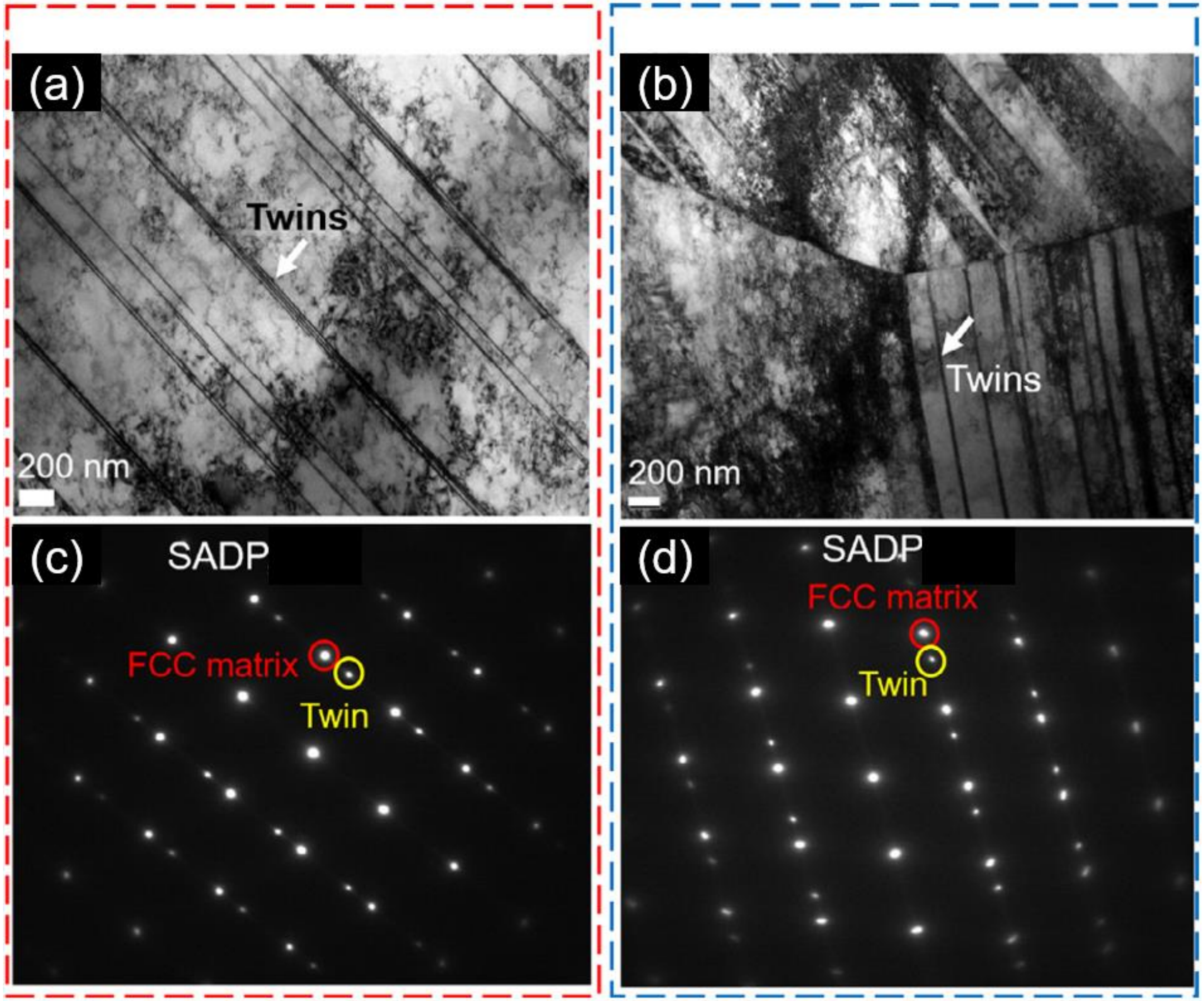

Source: Sabzi et al. 2022 [https://doi.org/10.1016/j.scriptamat.2021.114307]

Austenitic stainless steels

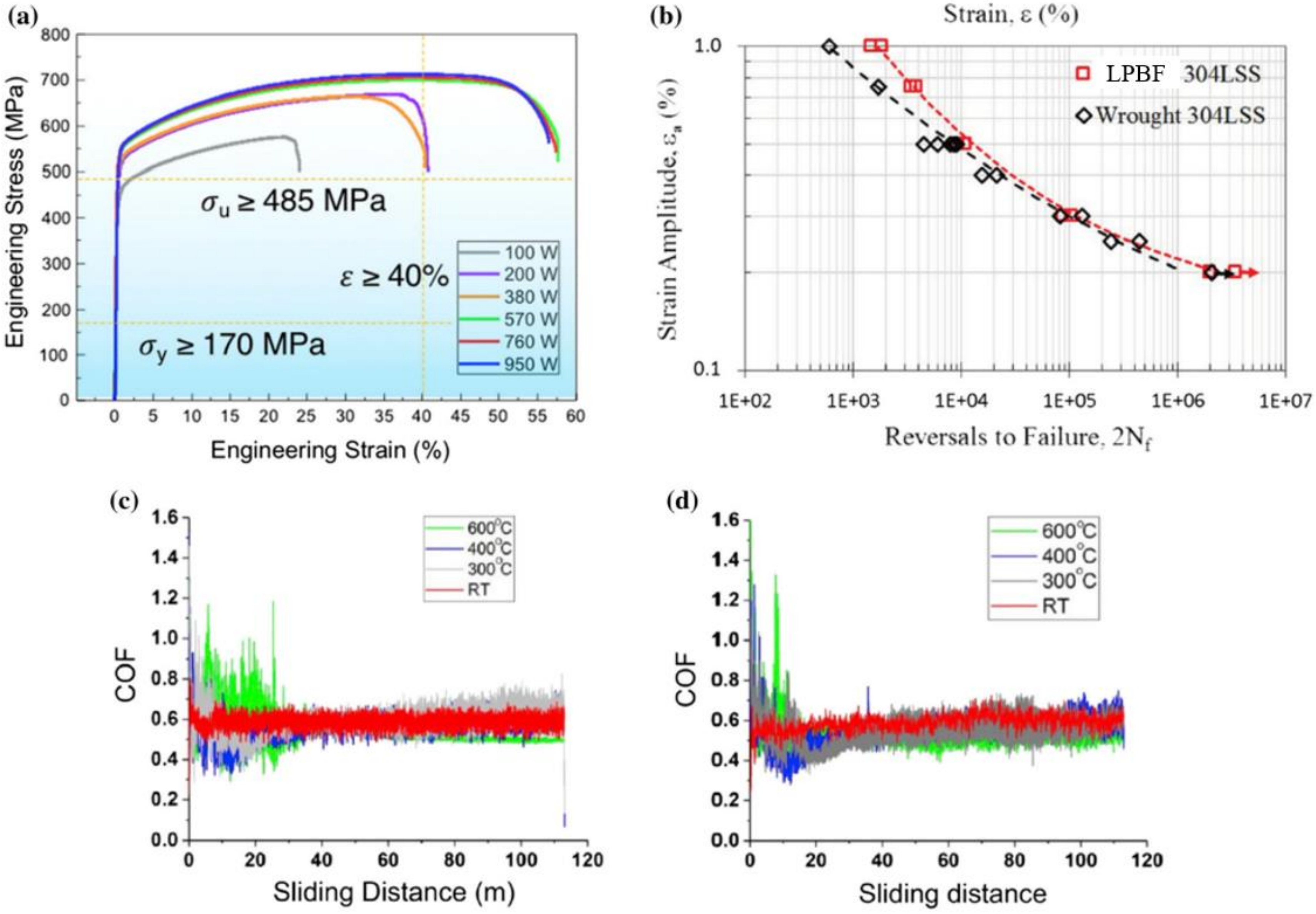

Fig. a) Tensile engineering stress-strain curve for LPBF 316L SS, The minimum tensile requirements for 316L SS are indicated by dashed yellow lines. b) The strain-life fatigue behavior of LPBF 304L austenitic SS and wrought 304L SS was compared. c) Wear behaviour of LPBF 316L SS after grinding (d) conventional 316L SS, demonstrating comparable wear resistance for LPBF 316L austenitic stainless steel at temperatures up to 400◦C.

Source: Haghdadi et al. 2021 [https://doi.org/10.1016/j.msea.2022.143882]

Austenitic stainless steels

Fig. (a) Representation of strengthening of LAGBs compared to HAGBs in LPBFed 316L SS. (b) Comparison of the Hall-Petch-type relationship obtained for LPBFed 316L SS with relationships reported for wrought 316L SS with various microstructures (CG: coarse grained, UFG: ultrafine grained and NG: nanograined).

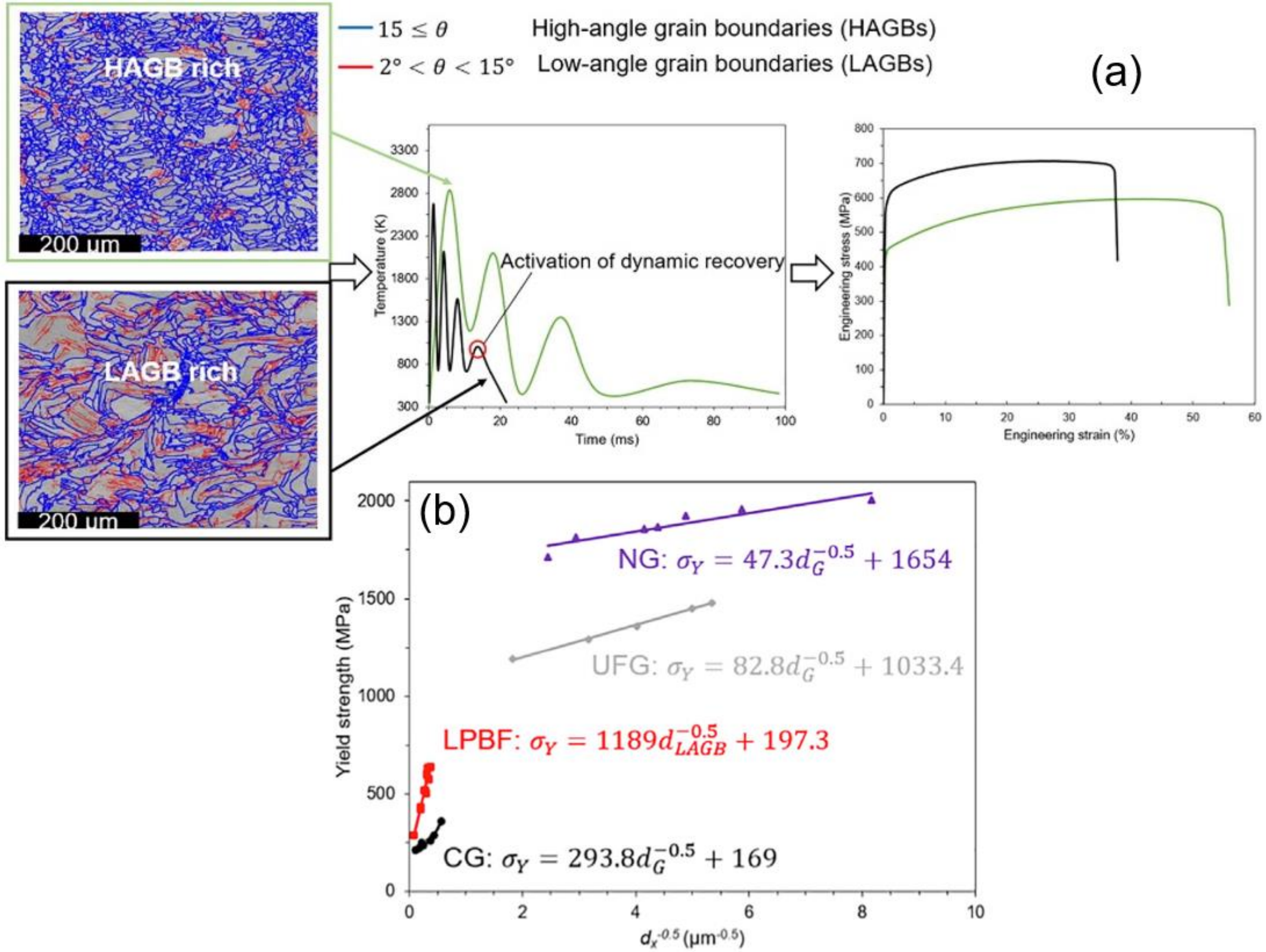

Source: Sabzi et al. 2021 [https://doi.org/10.1016/j.matdes.2021.110246]

Austenitic stainless steels

Fig. (a) Representative EBSD inverse pole figure (IPF) map showing a single crystalline 316L SS in the LPBF as-built state, which went through DRX after tensile deformation at room temperature, (b) and (c) Representative EBSD IPF maps showing DRX grains (black circles and arrows) after room temperature deformation in a polycrystalline LPBFed 316L SS (Red arrows show deformation twins along LAGBs), and (d) Representative bright field TEM micrograph showing DRX grains along grain boundaries (GB) after deformation of the same polycrystalline LPBFed 316L SS

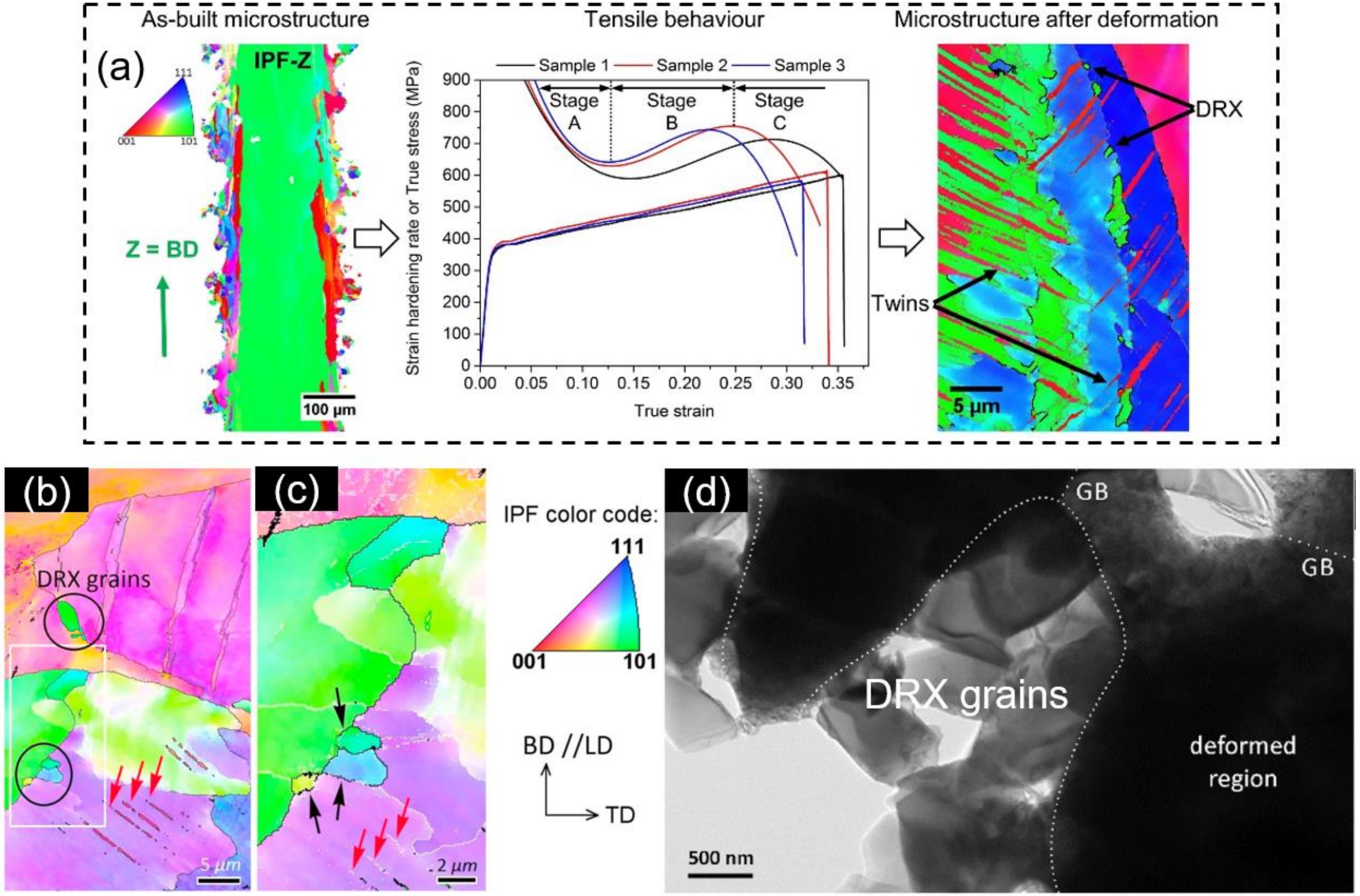

Source: [(a)] Wang et al. 2019 [https://doi.org/10.1016/j.scriptamat.2018.12.032]
[(b),(c),(d)] Heidarzadeh et al. 2021[https://doi.org/10.1016/j.msea.2021.141214]

Marageing steels

Fig. (a)-(d) Schematic depiction of the microstructure evolution in maraging steels during AM and subsequent ageing treatment. (e) A schematic thermal history of the sample by local laser/electron beam heating.
(As and Af denote austenite start and finish temperatures, respectively)

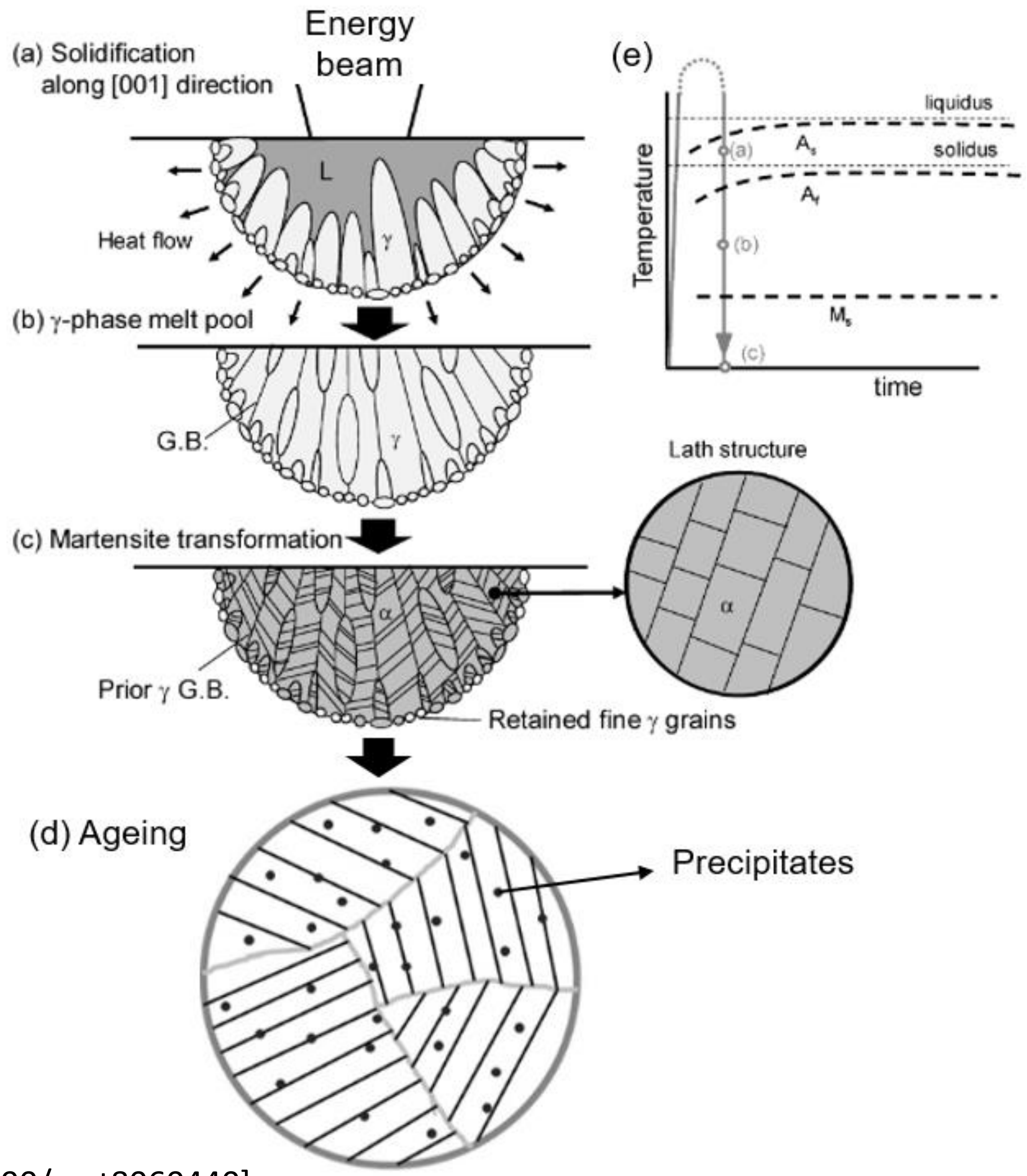

Source: Takata et al.2018 [https://doi.org/10.3390/met8060440]

Marageing steels

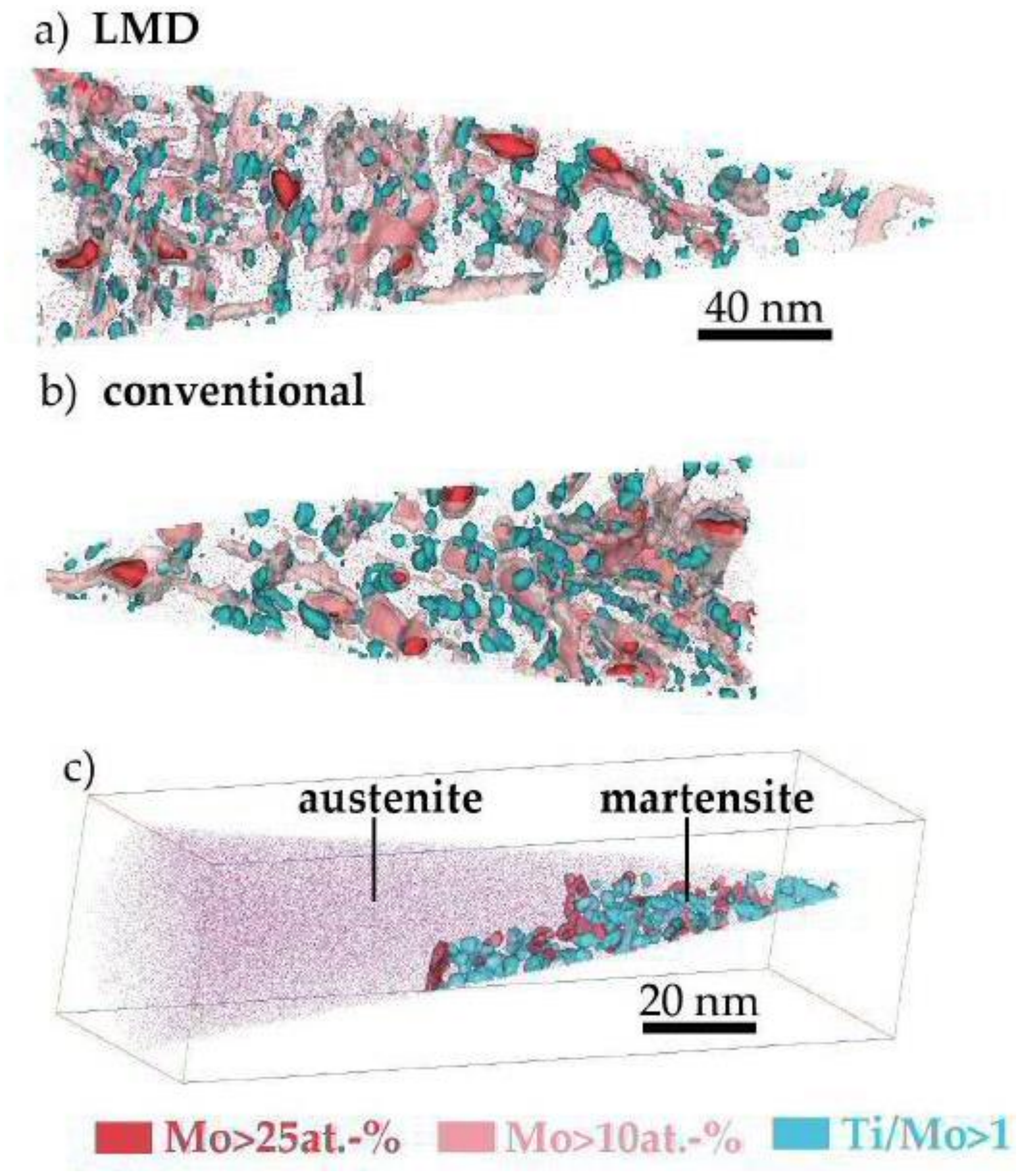

Fig. APT of (a) LMDed and (b) conventionally produced 18Ni-300 marageing steel after ageing heat treatment. Both materials contain three distinct types of precipitates, as indicated by three distinct iso-concentration surfaces. (c) APT microstructure section that includes both precipitate-containing martensite and precipitate-free austenite of LMDed 18Ni-300 marageing steel

Source: Jagle et al. 2017 [https://doi.org/10.3390/ma10010008]

Marageing steels

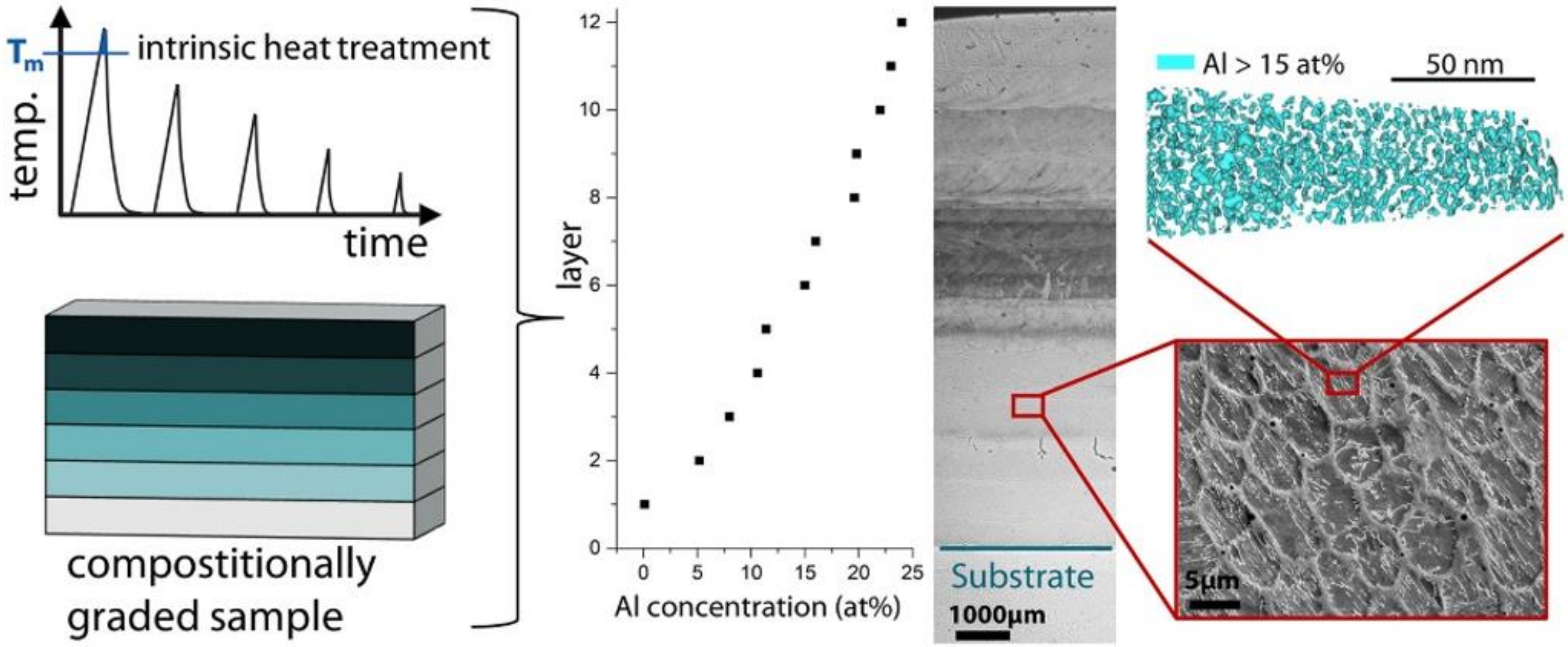

Fig. Fabrication of compositionally graded marageing steel with LMD as a result of intrinsic heat treatments. Al-rich precipitates were increased by the number of layers deposited on the previous layers. (T_m:melting temperature)

Source: Kurnsteiner et al. 2017 [https://doi.org/10.1016/j.actamat.2017.02.069]

Marageing steels

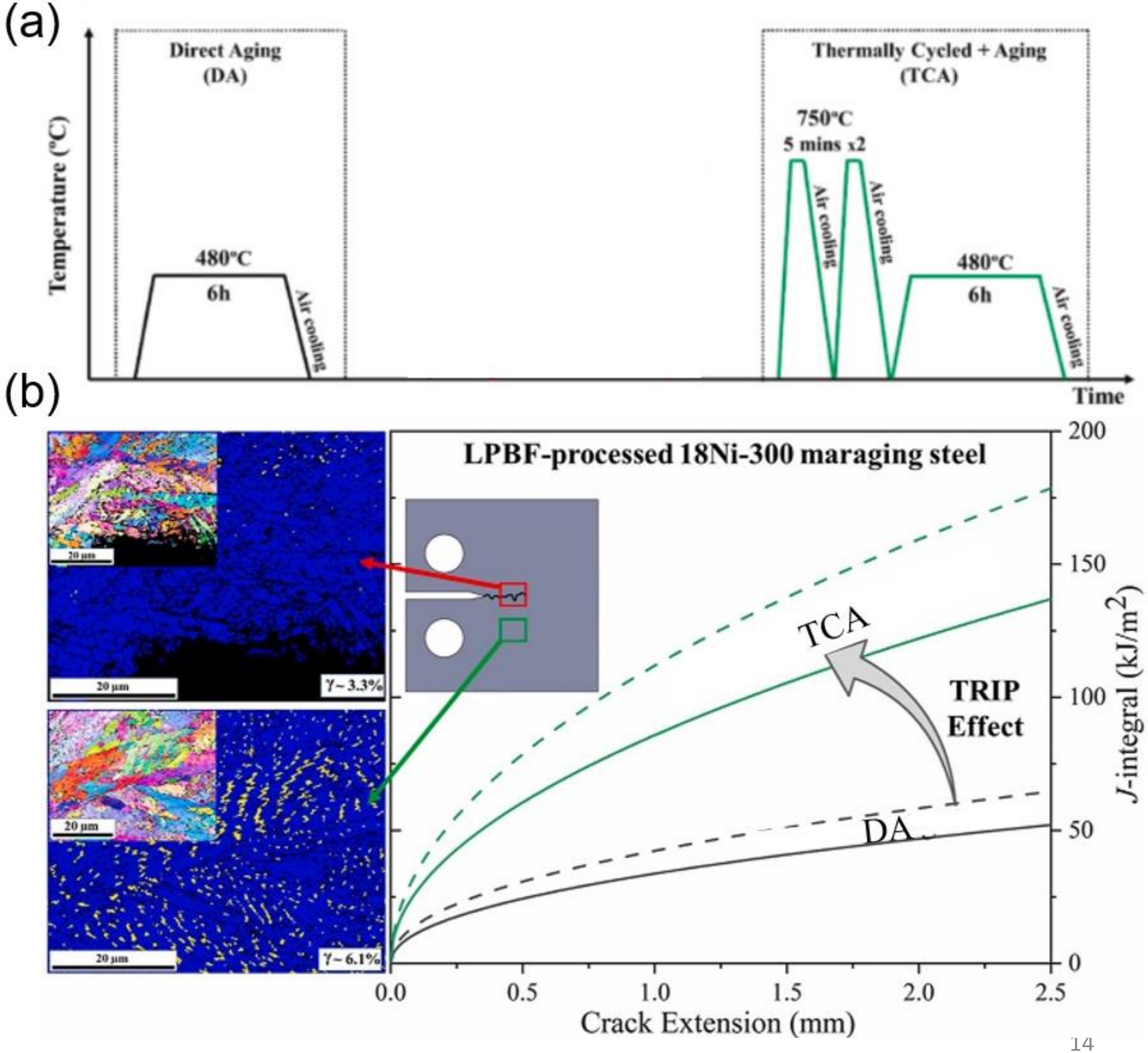

Fig. Toughness increase via TRIP effect promoted via thermal cycling and ageing: (a) Heat treatment routes and (b) crack resistance curves (J-integral) of the LPBFed 18Ni-300 marageing steels after two heat treatments as shown in (a)
(In the EBSD phase maps that are shown in (b), blue and yellow indicate martensite and austenite phases, respectively. In J-integral curves, the solid and dashed lines correspond to a crack propagating parallel and perpendicular to build direction, respectively)

Source: Paul et al. 2022 [https://doi.org/10.1016/j.msea.2022.143167]

Precipitation hardening stainless steels

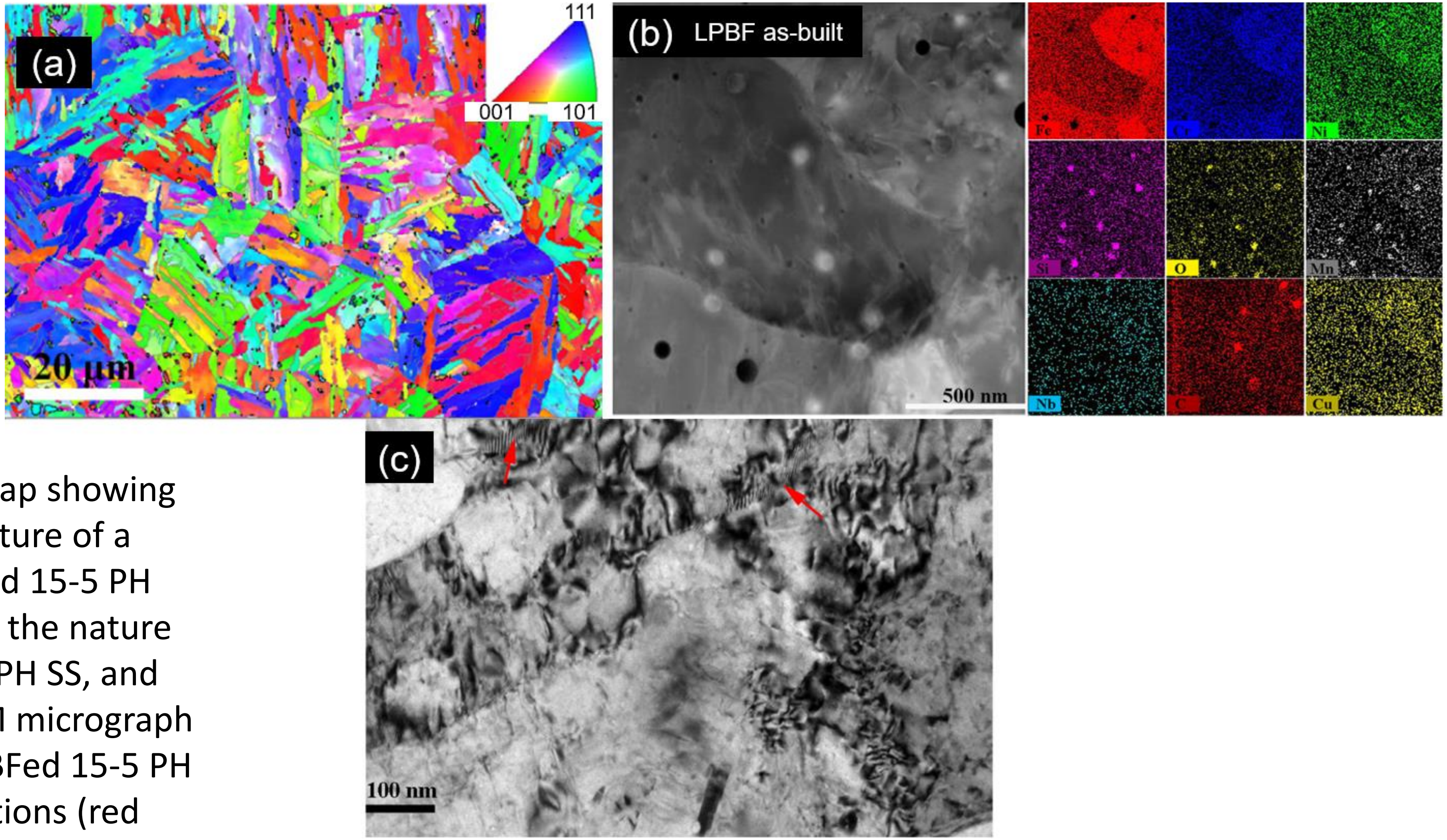

Fig. (a) Representative EBSD IPF map showing nearly fully martensitic microstructure of a solution annealed and aged LPBFed 15-5 PH SS, (b) STEM micrograph revealing the nature of inclusions in LPBF as-built 15-5 PH SS, and (c) Representative bright field TEM micrograph of solution annealed and aged LPBFed 15-5 PH SS showing the pile-ups of dislocations (red arrows) at the grain boundaries

Source: Nong et al. 2020 [https://doi.org/10.1016/j.scriptamat.2019.10.040]

Precipitation hardening stainless steels

Fig. (a) STEM representation of geometrically necessary dislocations in 17-4 PH SS in As-LPBF state. (b) EBSD analysis showing band contrast (BC), phase map of martensite (BCT phase in blue) and austenite (FCC phase in red), and the IPF maps of martensite (BCT) and austenite (FCC) in LPBF+Direct Ageing of 17-4 PH SS; (c)-(f) Represent schematics of microstructure-property in LPBFed 17-4 PH SS: (c) Fine packets of martensite (matrix) and reverted austenite with dispersed nano Mn and Si oxides. (d) Solution heat treatment (SHT) followed by water quenching increased martensite fraction and induced some Cu precipitation, (e) Ageing increased Cu-rich precipitates and induced some austenite reversion, and (f) Direct ageing after LPBF, which increased austenite reversion and induced some Cu-rich precipitates, and (g) Stress-strain tensile curves of cast and wrought (C&W) and LPBFed 17-4 PH SS.

$\sigma_{y,}\sigma_{UTS}$: yield and ultimate tensile strength, respectively

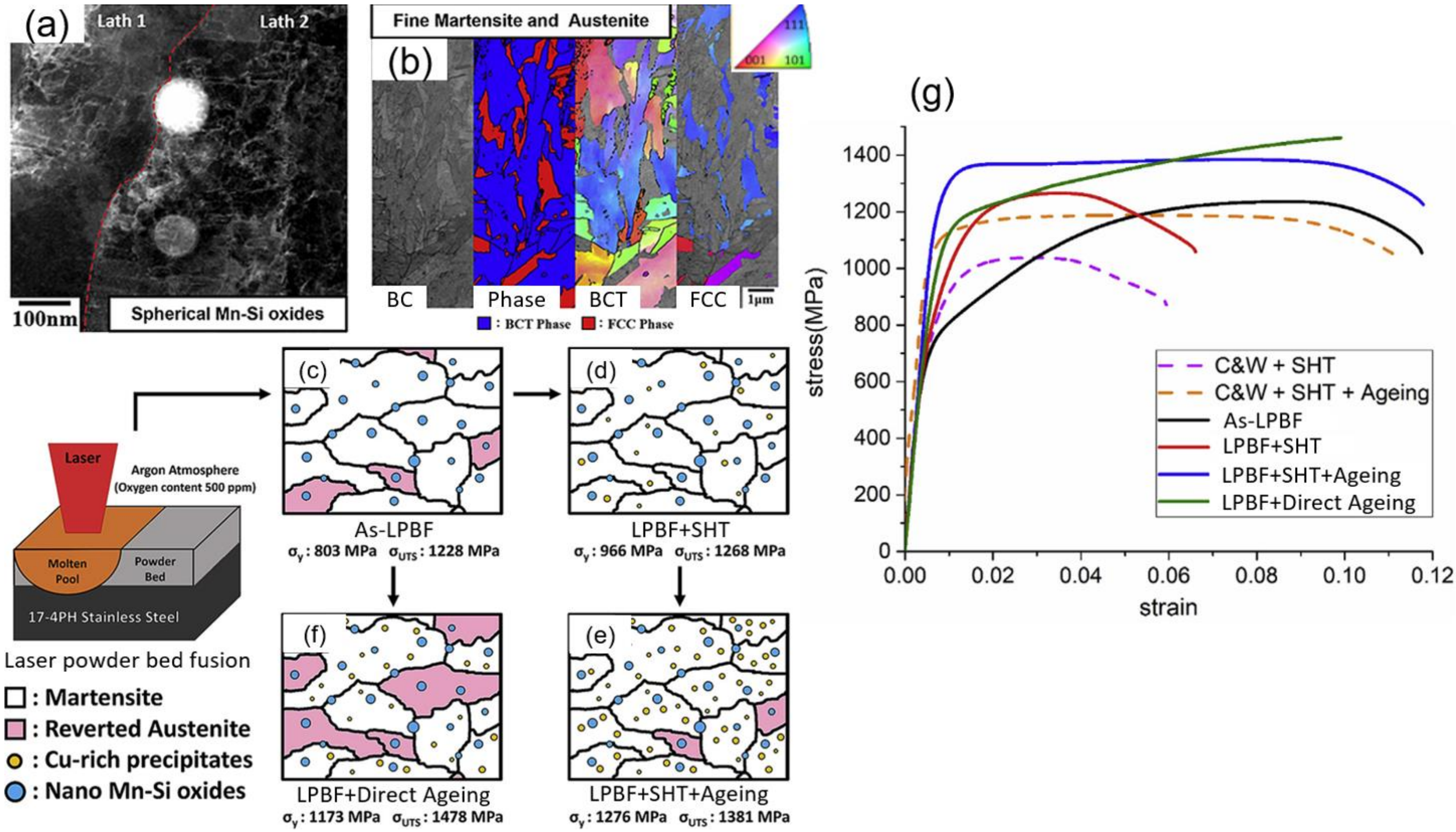

Source: Hsu et al. 2019 [https://doi.org/10.1016/j.jallcom.2019.06.289]

Tool steels

Fig. (a) The relative density of LPBFed H13 tool steel parts corresponding to volumetric energy density (E_v) for preheat and non-preheat conditions, (b)-(d) Representative optical micrographs showing pores and cracks in non-preheated samples with various E_v, (e)-(g) Representative optical micrographs showing no cracks in preheated samples with various E_v, and (h) and (i) Schematics of formation of compressive (blue arrows) and tensile (red arrows) residual stresses during LPBF layer deposition

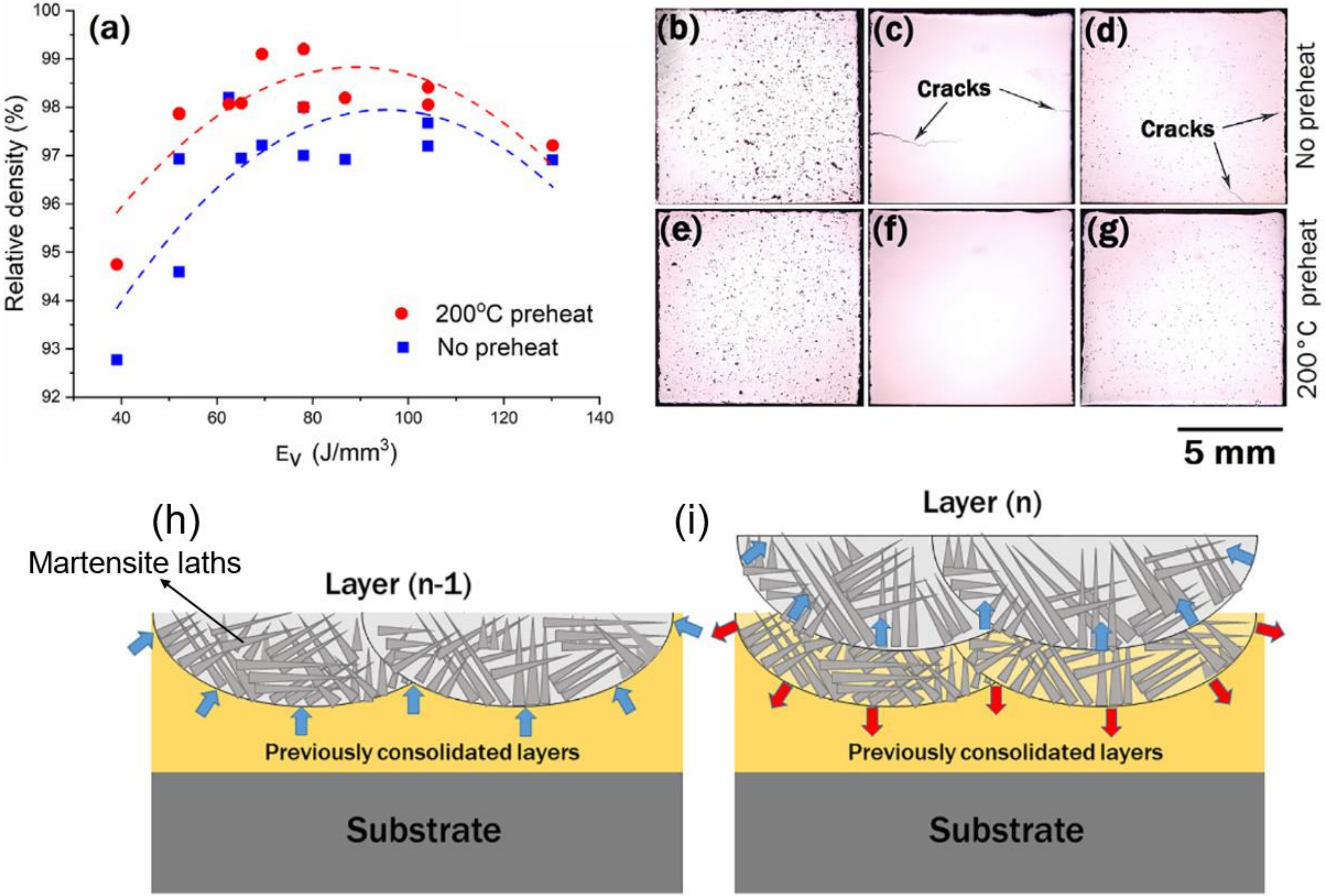

Source: Narvan et al. 2021 [https://doi.org/10.1016/j.matdes.2021.109659]

Duplex stainless steels

Fig. (a)EBSD phase map of the hot rolled (wrought) SAF2205 DSS. Austenite (γ) and α-ferrite are shown in red and blue, respectively, (b) SEM micrograph showing morphology of the gas atomised DSS, which has a ferritic structure, instead of duplex structure, due to the high cooling rates during gas atomisation. (c) LPBFed SAF2205, showing an almost fully ferritic microstructure shown in EBSD phase map. Austenite and δ-ferrite are shown in red and green, respectively. (d) Polarisation test results indicating similar corrosion behaviour of the LPBFed and wrought SAF2205 DSS. (e) Vickers hardness and specific wear rate of the LPBFed as-built and wrought SAF2205 DSS showing harder and more wear resistant LPBFed alloy.

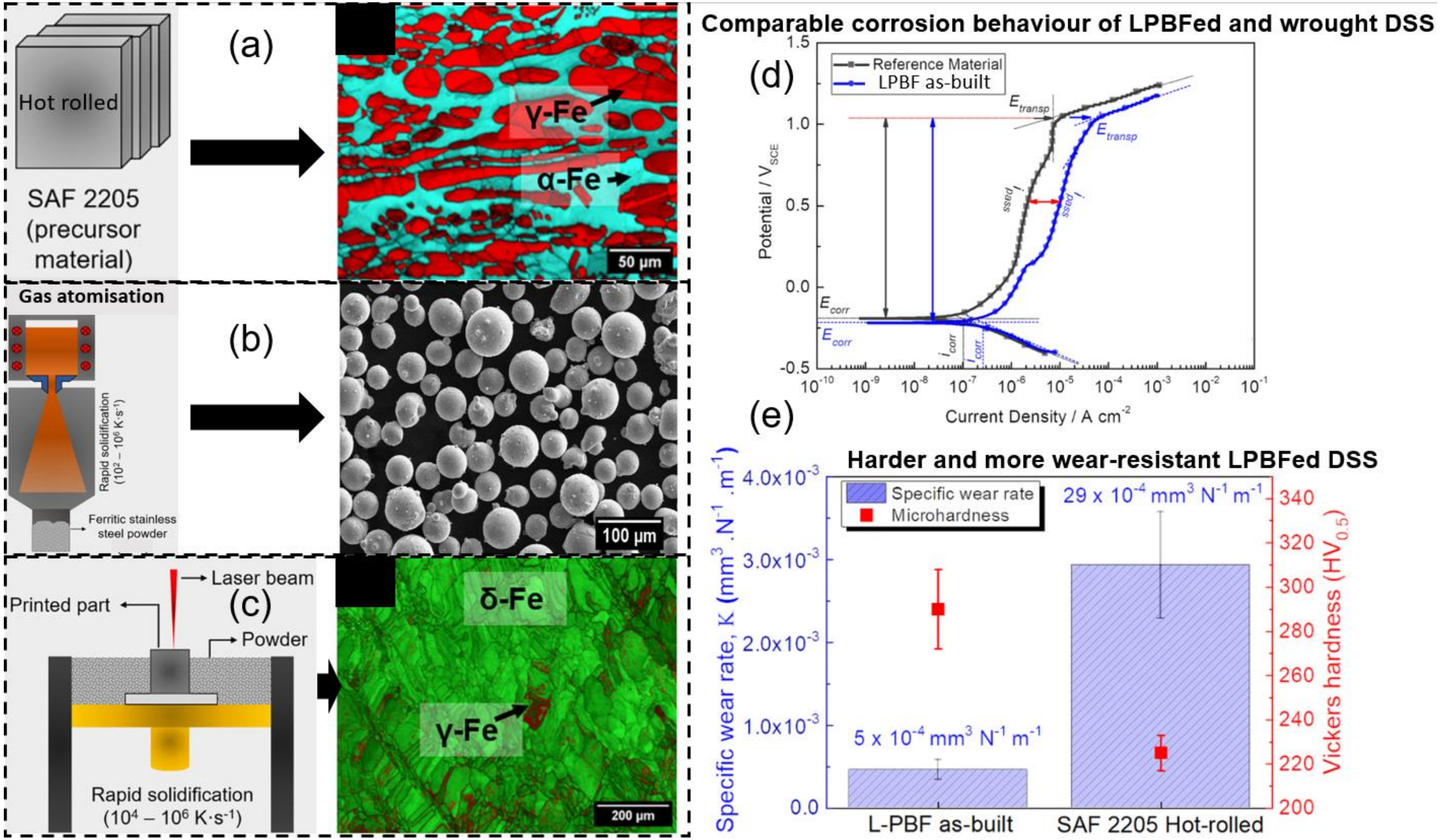

Source: Freitas et al. 2022 [https://doi.org/10.1016/j.jallcom.2022.165576]

Summary

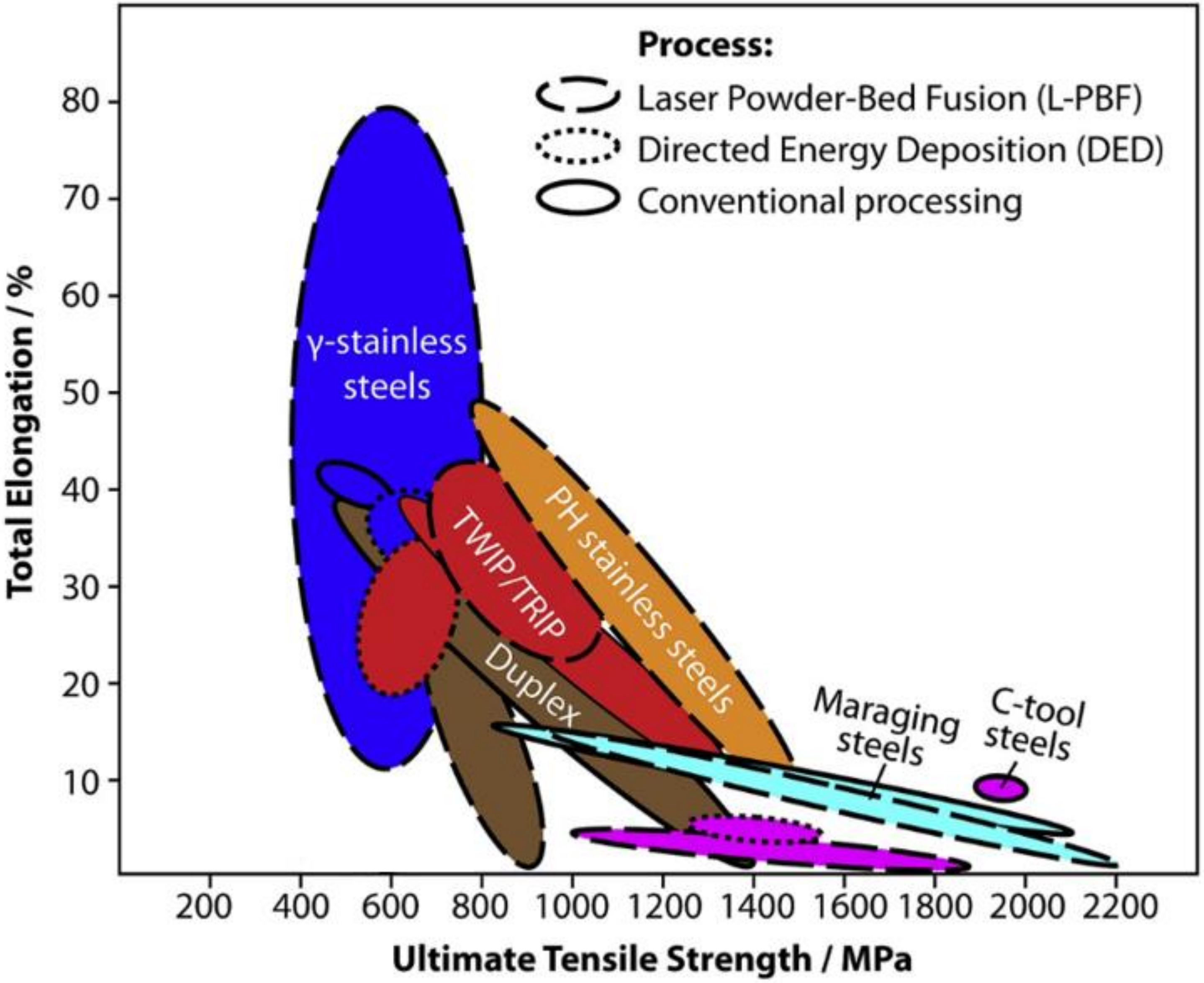

Fig. Overview of the mechanical properties of various steels produced by AM and conventional manufacturing

Source: Bajaj et al. 2020 [https://doi.org/10.1016/j.msea.2019.138633]

Summary

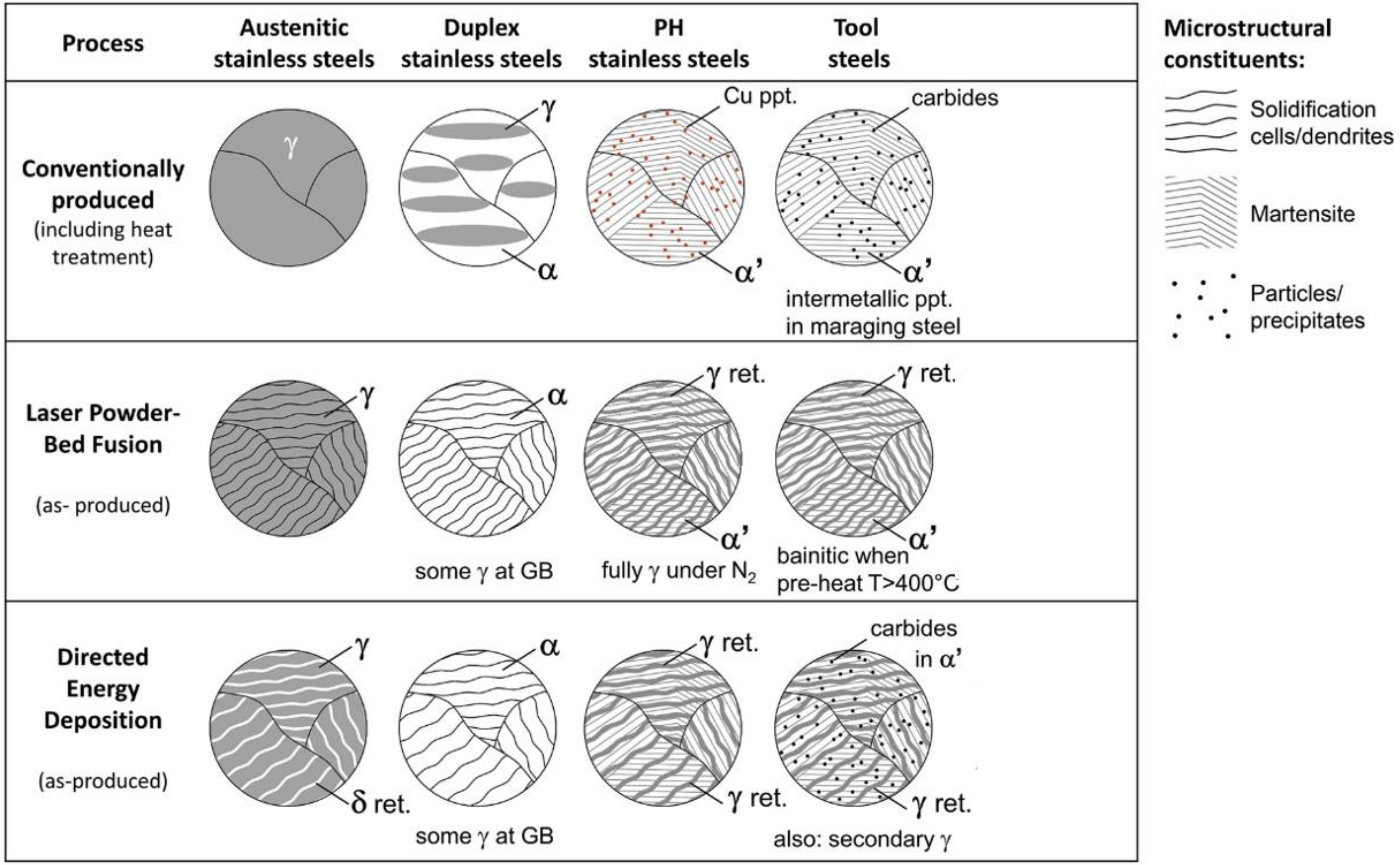

Fig. Schematic overview of the typical microstructures of various steels produced by AM and conventional manufacturing. ppt, γ ret., α, α′, γ, and GB denote precipitates, retained austenite, ferrite, martensite, austenite, and grain boundary, respectively

Source: Bajaj et al. 2020 [https://doi.org/10.1016/j.msea.2019.138633]